nature nanotechnology

LETTERS

PUBLISHED ONLINE: 5 JANUARY 2015 | DOI: 10.1038/NNANO.2014.313

Nanoscale NMR spectroscopy and imaging of multiple nuclear species

Stephen J. DeVience[1], Linh M. Pham[2], Igor Lovchinsky[3], Alexander O. Sushkov[1,3], Nir Bar-Gill[4], Chinmay Belthangady[2], Francesco Casola[2], Madeleine Corbett[5], Huiliang Zhang[3], Mikhail Lukin[3], Hongkun Park[1,3,6], Amir Yacoby[3,5] and Ronald L. Walsworth[1,2,3,6]*

Nuclear magnetic resonance (NMR) spectroscopy and magnetic resonance imaging (MRI) provide non-invasive information about multiple nuclear species in bulk matter, with wide-ranging applications from basic physics and chemistry to biomedical imaging[1]. However, the spatial resolution of conventional NMR and MRI is limited[2] to several micrometres even at large magnetic fields (>1 T), which is inadequate for many frontier scientific applications such as single-molecule NMR spectroscopy and *in vivo* MRI of individual biological cells. A promising approach for nanoscale NMR and MRI exploits optical measurements of nitrogen–vacancy (NV) colour centres in diamond, which provide a combination of magnetic field sensitivity and nanoscale spatial resolution unmatched by any existing technology, while operating under ambient conditions in a robust, solid-state system[3–5]. Recently, single, shallow NV centres were used to demonstrate NMR of nanoscale ensembles of proton spins, consisting of a statistical polarization equivalent to ~100–1,000 spins in uniform samples covering the surface of a bulk diamond chip[6,7]. Here, we realize nanoscale NMR spectroscopy and MRI of multiple nuclear species (^{1}H, ^{19}F, ^{31}P) in non-uniform (spatially structured) samples under ambient conditions and at moderate magnetic fields (~20 mT) using two complementary sensor modalities.

We interrogate single shallow NV centres in a diamond chip to perform simultaneous multi-species NMR spectroscopy and one-dimensional MRI on few-nanometre-sized samples placed on the diamond surface, which have a statistical spin polarization equivalent to ~100 polarized nuclei. We also use a diamond chip containing a shallow, high-density NV layer to demonstrate wide-field optical NMR spectroscopy and two-dimensional MRI with sub-micrometre resolution of samples containing multiple nuclear species. For all diamond samples exposed to air, we identify a ubiquitous ^{1}H NMR signal, consistent with a ~1 nm layer of adsorbed hydrocarbons or water on the diamond surface and below any sample placed on the diamond. This work lays the foundation for diverse NMR and MRI applications at the nanoscale, such as determination of the structure and dynamics of single proteins and other biomolecules, identification of transition states in surface chemical reactions, functional biological imaging with subcellular resolution and cellular circuit field of view, and characterization of thin films with sub-nanometre resolution.

The spatial resolution of conventional NMR and MRI is limited to macroscopic length scales due to the modest signal-to-noise ratio (SNR) provided by inductively detected thermal spin polarization, even in large (>1 T) magnetic fields, and the finite strength of the externally applied magnetic field gradients used for Fourier *k*-space imaging[2]. Other precision magnetic sensors have only macroscopic resolution (for example, semiconductor Hall effect sensors[8] and atomic magnetometers[9]) and/or require operation at cryogenic temperatures or in vacuum (for example, superconducting quantum interference devices (SQUIDs)[10] and magnetic resonance force microscopy (MRFM)[11,12]). Alternatively, NV centres in room-temperature diamond can be brought within a few nanometres of magnetic field sources of interest while maintaining long NV electronic spin coherence times (~100 μs), a large Zeeman shift of the NV spin states (~28 MHz mT^{-1}), and optical preparation and readout of the NV spin (Fig. 1a). Highlights of NV-diamond magnetic sensing to date (all performed under ambient conditions) include sensitive spectroscopy[13–15] and imaging[16–18] of electron and nuclear spin impurities within the diamond sample, single electron spin imaging external to the diamond sensor[19], sensing the aforementioned nanoscale NMR of proton spins in samples placed on the diamond surface[6,7,20], targeted detection of single paramagnetic molecules attached to the diamond surface[21], wide-field magnetic imaging of living magnetotactic bacteria, with sub-micrometre resolution[22], and the recent realization of single proton NMR and MRI for very shallow NV centres[23].

In the first NV-diamond sensor modality used in the present work (Fig. 1b), a scanning confocal microscope interrogates a single NV centre located a few nanometres below the surface of a high-purity diamond chip. In the second sensor modality (Fig. 1c), the fluorescence from a shallow (5–15 nm deep), high-density (3.5×10^{11} cm^{-2}) NV ensemble layer near the surface of a diamond chip is imaged onto a charge-coupled device (CCD) camera[24]. The NV ensemble wide-field microscope provides pixel-by-pixel multi-species NMR spectroscopy and two-dimensional MRI with sub-micrometre resolution and wide field of view, in a robust device that does not rely on identifying and addressing an optimally chosen NV centre, while the single NV confocal microscope can extract thickness information of layered thin films containing different nuclear species, with sub-nanometre resolution.

For both sensor modalities, an NV NMR measurement proceeds in the following way. First, an 8-μs-long 532 nm laser pulse optically pumps the NV electronic spins into the $|0\rangle$ state. Resonant microwave pulses are then applied to the NV electronic spins. First, a $\pi/2$ pulse prepares a coherent superposition of ground spin states

---

[1]Department of Chemistry and Chemical Biology, Harvard University, 12 Oxford Street, Cambridge, Massachusetts 02138, USA. [2]Harvard-Smithsonian Center for Astrophysics, 60 Garden Street, Cambridge, Massachusetts 02138, USA. [3]Department of Physics, Harvard University, 17 Oxford Street, Cambridge, Massachusetts 02138, USA. [4]Department of Applied Physics and Racah Institute of Physics, Hebrew University, Edmond J. Safra Campus, Jerusalem, Israel. [5]School of Engineering and Applied Sciences, Harvard University, 15 Oxford Street, Cambridge, Massachusetts 02138, USA. [6]Center for Brain Science, Harvard University, 52 Oxford Street, Cambridge, Massachusetts 02138, USA. *e-mail: rwalsworth@cfa.harvard.edu

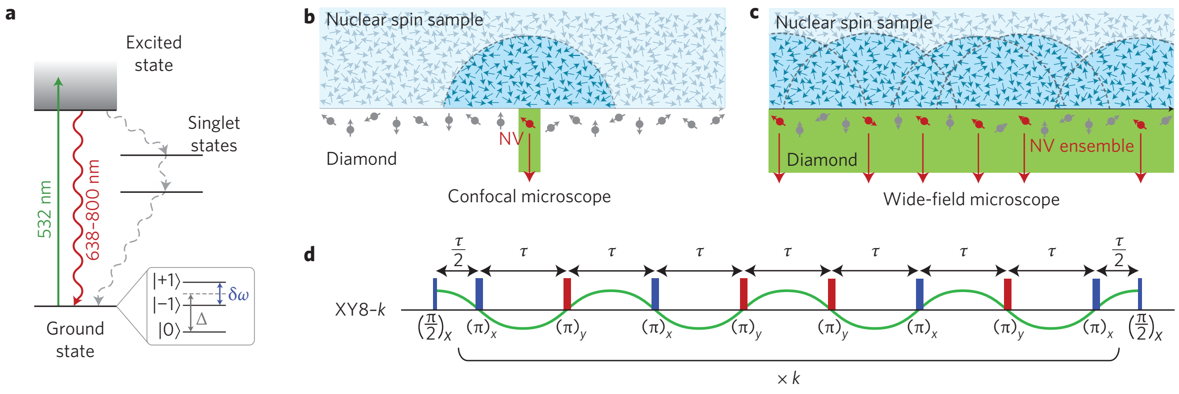

Figure 1 | NV NMR experiment. **a**, NV centre energy level diagram (see Supplementary Methods for details). **b**, A confocal microscope interrogates a single shallow NV centre, which detects NMR signals from a few-nanometre region of sample on the diamond surface. **c**, A wide-field microscope images fluorescence from a shallow, high-density layer of NV centres allowing detection of NMR signals from overlapping nanoscale regions of sample on the diamond surface. Only NV centres of the same orientation (shown in red), aligned along an externally applied static magnetic field, B_0, contribute to the ensemble NV NMR signal. **d**, Larmor precessing nuclear spins in the sample produce an effective a.c. magnetic field (such as the one shown by the green line) that is detected by NV sensors in a frequency-selective manner using an XY8-k pulse sequence.

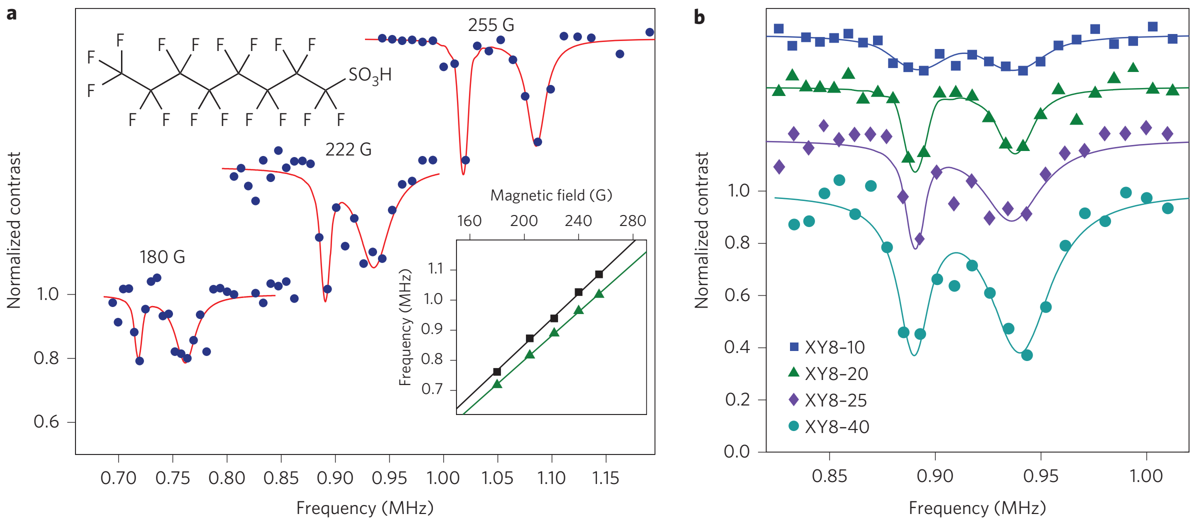

Figure 2 | Multi-species nanoscale NMR with a single shallow NV centre. **a**, ^{1}H and ^{19}F NMR spectra of a fluorinated sample (PFOS/POSF) under several magnetic fields, measured with an XY8-30 sequence and fit with a model for the NV NMR lineshape. Top inset: Schematic of PFOS molecular structure. Bottom inset: Measured ^{1}H and ^{19}F NMR resonance frequencies as a function of applied static magnetic field B_0. Error bars are smaller than the markers. Linear fits yield gyromagnetic ratios γ matching the literature values within experimental error, with the standard deviation in γ determined from the linear fit. Black squares, ^{1}H $\gamma = (4.257 \pm 0.014)$ kHz G^{-1}; green triangles, ^{19}F $\gamma = (4.003 \pm 0.007)$ kHz G^{-1}. **b**, Series of NV NMR spectra for the fluorinated sample acquired with an increasing number of repetitions k of the XY8-k pulse sequence. Measurement sensitivity and spectral selectivity improve with increased repetitions k. Note: in both **a** and **b**, spectra are offset vertically for clarity.

$(|0\rangle + |1\rangle)/\sqrt{2}$. Then, an XY8–$k$ sequence allows the NV spins to probe the local magnetic environment[25]. Finally, a $\pi/2$ pulse projects the evolved NV spin coherence onto a $|0\rangle,|1\rangle$ state population difference, which is detected via the NV spin-state dependent fluorescence intensity after a 500 ns, 532 nm laser pulse. The XY8–k pulse sequence consists of a block of eight sequential π-rotation pulses repeated k times (Fig. 1d) and serves two purposes. First, the sequence dynamically decouples NV spins from the background magnetic environment (for example, spin impurities in diamond and other sources of magnetic noise) so that the NV spin coherence time T_2 is extended beyond the inhomogeneous dephasing time T_2^* and the single Hahn-echo coherence time[26–30]. Second, the XY8–k sequence gives the NV spins narrow-band sensitivity to NMR signals centred at frequency $\nu = 1/2\tau$ (where τ is the delay time between π pulses) and with detection bandwidth $\Delta\nu = 0.111/k\tau$ (refs 14,31,32). The presence of an NMR signal resonant with the XY8–k sequence is detected as a spectrally specific change in the NV optical fluorescence signal (see Supplementary Methods for details).

Importantly, the strength of the NV NMR signal and the number of nuclear spins detected per NV are sensitively dependent on the NV depth and the density of nuclear spins in the sample[20]. To calibrate NV depth, we used NV NMR measurements from protons in immersion oil (a well-understood sample with uniform ^{1}H density) placed on the diamond surface, together with a model of magnetic field fluctuations at each NV centre induced by the ensemble of statistically polarized nuclear spins in the sample (L. M. Pham *et al.*, manuscript in preparation). We used the resulting NV depth and the nuclear magnetic field model to determine the number of nuclear spins sensed in each sample studied. Details of the NV depth calibration are given in the Supplementary Methods (L. M. Pham *et al.*, manuscript in preparation).

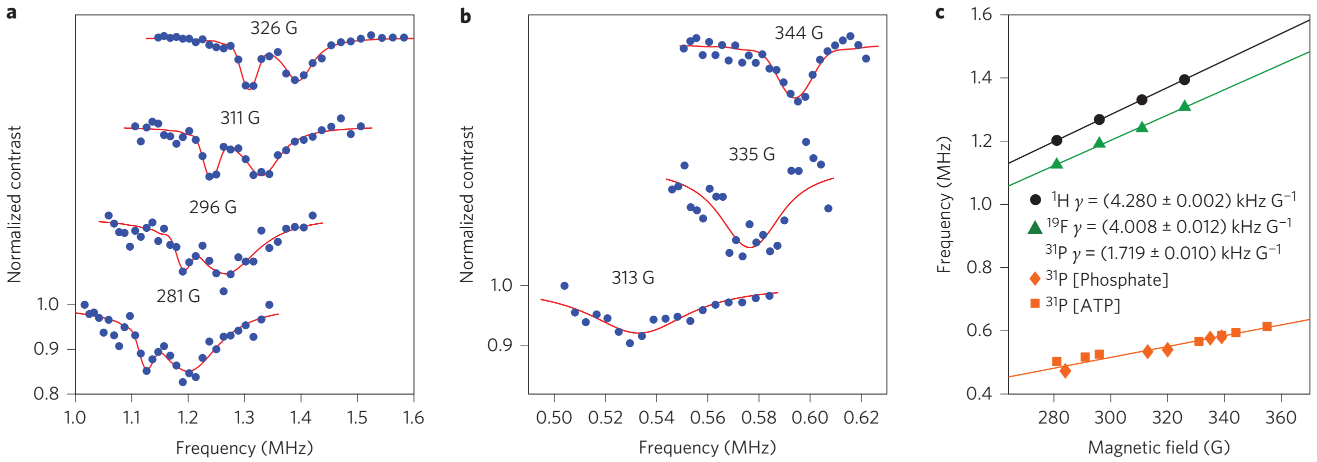

Figure 3 | Multi-species nanoscale NMR with a shallow NV ensemble. a, Example NMR spectra of a fluorinated sample (PFOS/POSF) at several magnetic fields, measured with an XY8–10 sequence. As with single-NV measurements, both ^{1}H and ^{19}F NMR signals are observed and fit with a model lineshape. **b**, Example ^{31}P NMR spectra from a dry disodium phosphate sample (at 313 and 335 G) and a powdered ATP sample (at 344 G) with an XY8–10 sequence, smoothed and fit with the model lineshape. Note: in both **a** and **b**, spectra are offset vertically for clarity. **c**, Measured ^{1}H, ^{19}F and ^{31}P NMR resonance frequencies as a function of applied static magnetic field B_0. Error bars are smaller than the markers. Linear fits yield gyromagnetic ratios γ matching the literature value within experimental error, with the standard deviation in γ determined from the linear fit.

Figure 2 presents example results for multi-species nanoscale NMR spectroscopy using a single NV centre, selected from a thin layer with average NV centre depth of 10 ± 2.6 nm. We placed a mixture of sodium perfluorooctanesulphonate (PFOS) and perfluorooctanesulphonyl fluoride (POSF) feedstock on the diamond surface and allowed it to dry under ambient conditions. Using an XY8–30 pulse sequence, we then measured NV NMR spectra of the fluorinated residue and observed resonances corresponding to ^{19}F and ^{1}H nuclei over a range of applied static magnetic fields, B_0, oriented along the NV axis. Several representative NMR spectra are shown in Fig. 2a, where we fit the measured NV fluorescence to a model function to extract the frequencies and linewidths of the NMR resonance dips (see Supplementary Methods and L. M. Pham *et al.*, manuscript in preparation, for details). For the ^{19}F NMR resonance, we determined that 50% of the observed NV NMR signal results from ~20,000 unpolarized fluorine nuclei in an ~(10 nm)^3 volume, which has a statistical spin polarization equivalent to ~140 polarized fluorine nuclei. In Fig. 2a we also plot the measured resonance frequency ν_0 of each nuclear species as a function of B_0, with an observed linear dependence $\nu_0 = (\gamma_n/2\pi)B_0$ that is consistent with the known gyromagnetic ratios of ^{19}F and ^{1}H (ref. 33).

To characterize the inhomogeneous dephasing time T_2^* for each nuclear species, we varied the number of repetitions k in the XY8–k pulse sequence and observed the effect on the measured NV NMR resonance features. As shown in Fig. 2b, we found that increasing k, and thereby creating a narrower spectral filter for the NV NMR measurement, results in a narrowing and deepening of the resonance dips, setting lower limits of $T_2^* \geq 32$ μs for ^{19}F and $T_2^* \geq 11$ μs for ^{1}H for this nanoscale sample on the diamond surface. As the number of pulses is increased, the measured linewidth approaches a limit set by $1/\pi T_2^*$, which results from field inhomogeneities, spin–spin interactions and diffusion. The linewidth measurement is also affected by the accumulation of pulse errors and decreasing SNR. Fluorine exhibits a longer T_2^* than protons because its lower gyromagnetic ratio produces weaker spin–spin interactions and because the larger molecular size of PFOS results in less diffusion.

As shown in Fig. 3, we also acquired consistent multi-species nanoscale NMR spectra using an ensemble of high-density, shallow-implanted NV centres in a wide-field microscope set-up, with the NV fluorescence signal detected by a CCD camera and integrated across the few-micrometre-wide laser spot. For this diamond chip, the mean lateral distance between NV centres of the same orientation is ~30 nm (determined from the NV fabrication process and wide-field fluorescence measurements), and the mean NV depth is ~10 nm (determined by the calibration process outlined above). In particular, the results in Fig. 3 demonstrate that high-sensitivity nuclear spin sensing can be provided by NV ensembles, without choosing an optimal single NV sensor. In the first example (Fig. 3a), we again measured a fluorinated sample (PFOS/POSF) dried on the diamond surface. Both ^{1}H and ^{19}F NMR signals are resolved, albeit with broader linewidths than observed for the single NV centre data of Fig. 2 due to magnetic field inhomogeneities across the laser spot. In the second example (Fig. 3b), we performed NV NMR measurements of ^{31}P nuclei for samples of dried disodium phosphate and powdered adenosine triphosphate disodium (ATP) salt on the diamond surface. In all ensemble measurements, the dip in fluorescence contrast is weaker than the single NV case due to background fluorescence from off-axis NV centres, which fluoresce but are not manipulated by the microwave pulses. Plots of the measured ^{1}H, ^{19}F and ^{31}P resonance frequencies versus magnetic field (Fig. 3c) are in agreement with the known gyromagnetic ratios of these nuclear species[33].

We next used the wide-field NV microscope to demonstrate two-dimensional optical MRI of spatially varying concentrations of ^{19}F nuclear spins, again using the fluorinated sample (PFOS/POSF). We fabricated a patterned structure (mask) of SiO_2 on the diamond surface via atomic-layer deposition. This structure covered part of the diamond surface, with a sub-micrometre edge going from the full thickness of the SiO_2 layer (90 nm) to bare diamond. Figure 4a shows a white light image of a corner defined by this structure. We introduced the fluorinated sample onto the diamond surface and applied the sensing protocol described above, which provided an NMR spectrum for each pixel of the CCD camera: that is, optical MRI with a lateral resolution of ~500 nm, a 50 μm field of view, and sensitivity to nuclear spins within ~20 nm of the diamond surface. An example ^{19}F NMR image is shown in Fig. 4b, with single-pixel NMR spectra on the bare diamond surface and under the SiO_2 structure shown in Fig. 4c. An additional example of data acquired near a different

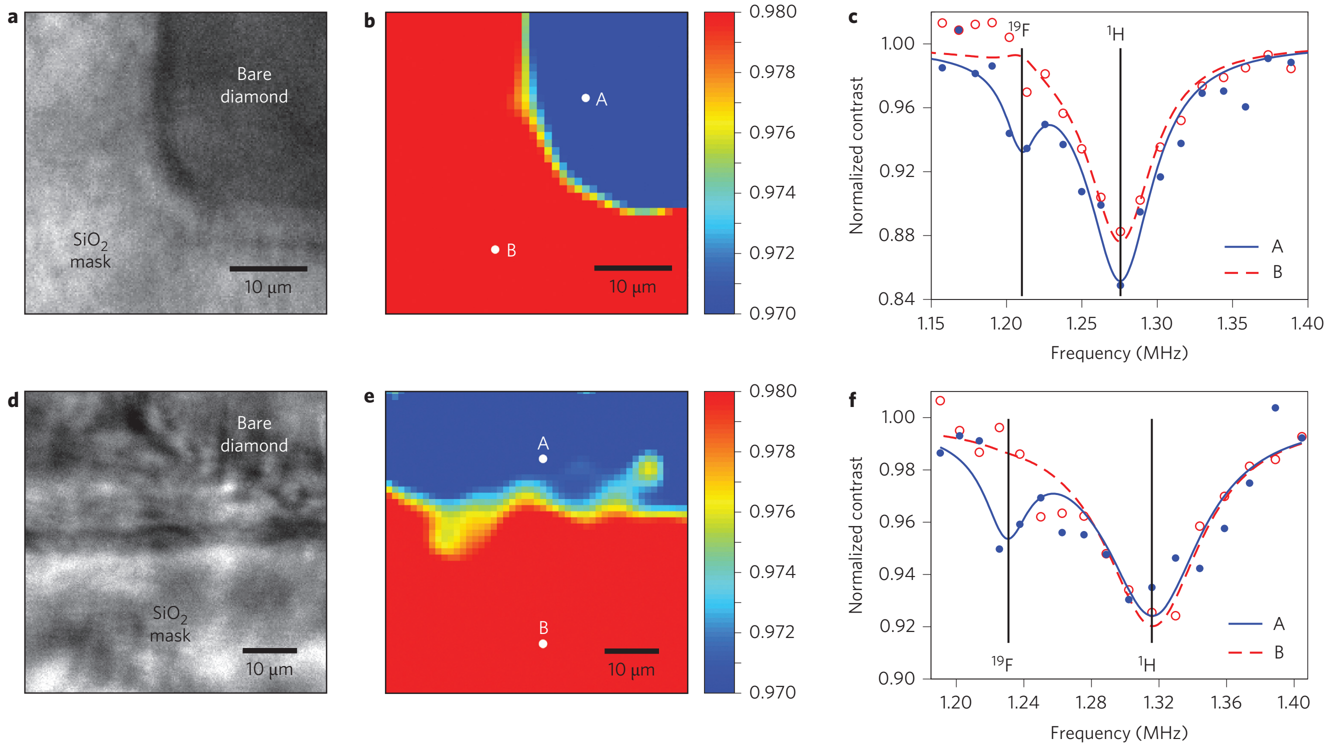

Figure 4 | Optical MRI of multi-species sample with sub-micrometre structure. a, White-light transmission image of shaped SiO_2 structure (90-nm-thick mask) on the surface of a diamond containing a shallow, high-density NV layer. **b**, Optical MRI of ^{19}F nuclear spin density in the fluorinated sample (PFOS/POSF) within ~20 nm of the surface. Colour indicates NMR contrast, with blue representing a deep ^{19}F NMR contrast dip and hence high fluorine concentration on the bare diamond surface as measured by the NV ensemble. Red represents no ^{19}F NMR signal detected by the NV ensemble under the SiO_2 layer. **c**, NV NMR spectra for two points (A and B) of the image in **b**, fit with Lorentzian curves. **d–f**, White-light transmission image, optical MRI of ^{19}F nuclear spin density, and NV NMR spectra of a second SiO_2 structure. On the bare diamond surface (A), NMR signals are observed for both ^1H and ^{19}F. Under the SiO_2 structure (B), only ubiquitous surface layer ^1H spins are detected, as the SiO_2 layer displaces the fluorinated sample ~90 nm away from the diamond surface and NV sensors.

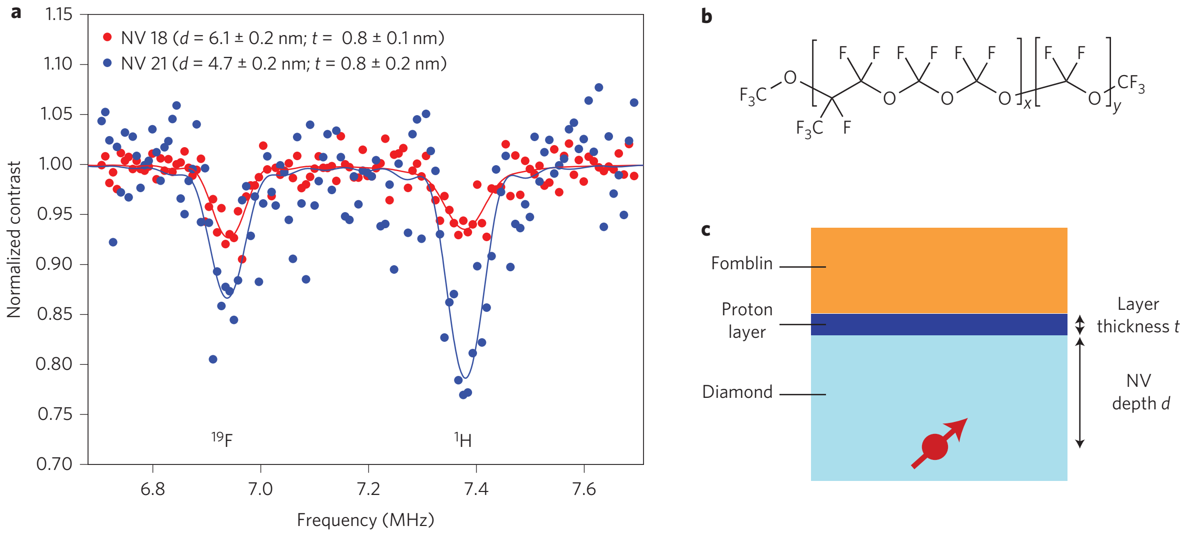

Figure 5 | Determination of surface proton layer thickness. a, NMR signal from Fomblin Y oil on the diamond surface measured with two NV centres separated by ~5 μm. NV depths are presented, as calculated from the lineshape model (see Supplementary Methods). **b**, Chemical structure of Fomblin Y oil. **c**, Description of the hypothesized sample structure resulting from Fomblin Y oil floating above a thin layer of adsorbed hydrocarbons or water on the diamond surface.

edge of the SiO_2 structure is shown in Fig. 4d–f. See Supplementary Methods for details. The SiO_2 structure prevented underlying NV centres from detecting the NMR signal from ^{19}F nuclear spins in the sample, due to the strong ($1/d^3$) distance dependence of NV sensitivity to magnetic dipole fields. In contrast, the NV centres remained sensitive to ^{19}F nuclear spins in the sample on the bare diamond surface. Note that a ^1H NMR signal was observed across the full diamond surface even under the SiO_2 structure, consistent with other recent observations using NV diamond[6,7,20] (H. J. Mamin, personal communication, May 2014) and MRFM[12,34,35]. These results illustrate the ability of our technique to provide nuclear-species-specific spectroscopic and imaging information for nanoscale samples across a wide field of view.

Finally, we used the single NV confocal microscope to investigate the origin of the ubiquitous ^{1}H NMR signal, observed on all diamond samples after extended exposure to air (including single NV and NV ensemble measurements), as well as in the presence of the dried PFOS/POSF sample and the SiO_2-coated region of the diamond. We applied Fomblin Y HVAC 140/13 oil, which contains ~40 ^{19}F nuclei per nm^3 and no ^{1}H, to the surface of a diamond directly after acid cleaning (see Supplementary Methods). NV NMR measurements of the Fomblin oil yield strong NMR signals of both ^{19}F and ^{1}H nuclei for each of several NV centres probed (see example data in Fig. 5a and the Supplementary Information). The different relative strengths of the ^{19}F and ^{1}H signals, dependent on the depth of the probed NV centre (previously calibrated as described in the Supplementary Methods and L. M. Pham *et al.*, manuscript in preparation), are consistent with a thin adsorbed hydrocarbon or water layer on the diamond surface and below the thick layer of Fomblin oil (Fig. 5b,c). Applying the NV NMR lineshape model to this hypothesized sample geometry yields a proton-containing layer thickness of ~1 nm, which is found to be very similar for proximal NV centres located within a few micrometres of each other. The data are not consistent with an isotropic mixture of Fomblin and proton-containing molecules, which would result in ^{1}H and ^{19}F spectral signals having the same relative strengths for proximal NV centres. This experiment and analysis represents a form of nanoscale one-dimensional MRI, and it provides the first proof-of-principle demonstration of the capability of the NV NMR technique to extract thickness information for multi-layered thin films containing multiple nuclear spin species, with sub-nanometre resolution.

In summary, we demonstrated a new capability for nanoscale, optically detected NMR spectroscopy and MRI of multiple nuclear species (^{1}H, ^{19}F, ^{31}P) using shallow NV centres in diamond. We performed simultaneous multi-species NMR spectroscopy under ambient conditions, using two experimental modalities: (1) a scanning confocal microscope interrogating single NV centres, which is suitable for probing few-nanometre-sized samples containing ~100 polarized nuclear spins as well as extracting thickness information for multiple layers of thin films with sub-nanometre resolution; and (2) a wide-field microscope using a CCD camera to image fluorescence from a high-density NV ensemble in a thin layer near the diamond surface, which is optimal for NMR spectroscopy and imaging over a >10 µm field of view and with sub-micrometre resolution. Importantly, the NV ensemble results show that high-sensitivity nanoscale NMR does not require choosing an optimal single NV sensor. These complementary NV sensor modalities provide utility well beyond current NMR and MRI technology, opening the door to wide-ranging applications at the nanoscale, from studies of surface catalyst reactions to the identification of single protein structure and dynamics to functional MRI within living cells. Future challenges for NV NMR and MRI include improving the sensitivity at the single nuclear spin level, and achieving both atomic-scale (ångstrom) spatial resolution and hertz-scale spectral resolution sufficient to observe chemical shifts in single biomolecules at low magnetic fields. Possible approaches to these problems include reliable creation of very shallow NV centres with good optical and spin properties[20], using Fourier *k*-space imaging techniques with pulsed magnetic field gradients of ~1 G nm^{-1} (refs 19,36) and exploiting quantum-assisted techniques such as 'reporter' electron spins on the diamond surface coherently coupled to a shallow NV[23] and ancilla nuclear spins as a quantum memory[37].

Received 13 June 2014; accepted 27 November 2014;
published online 5 January 2015; corrected online
16 January 2015

References

1. Mansfield, P. Snapshot magnetic resonance imaging (Nobel lecture). *Angew. Chem. Int. Ed.* **43,** 5456–5464 (2004).
2. Glover, P. & Mansfield, P. Limits to magnetic resonance microscopy. *Rep. Progr. Phys.* **65,** 1489 (2002).
3. Taylor, J. M. *et al.* High-sensitivity diamond magnetometer with nanoscale resolution. *Nature Phys.* **4,** 810–816 (2008).
4. Maze, J. R. *et al.* Nanoscale magnetic sensing with an individual electronic spin in diamond. *Nature* **455,** 644–647 (2008).
5. Balasubramanian, G. *et al.* Nanoscale imaging magnetometry with diamond spins under ambient conditions. *Nature* **455,** 648–651 (2008).
6. Mamin, H. J. *et al.* Nanoscale nuclear magnetic resonance with a nitrogen vacancy center. *Science* **339,** 557–560 (2013).
7. Staudacher, T. *et al.* Nuclear magnetic resonance spectroscopy on a (5-nanometer)^3 sample volume. *Science* **339,** 561–563 (2013).
8. Bending, S. J. Local magnetic probes of superconductors. *Adv. Phys.* **48,** 449–535 (1999).
9. Budker, D. & Romalis, M. Optical magnetometry. *Nature Phys.* **3,** 227–234 (2007).
10. Nowack, K. C. *et al.* Imaging currents in HgTe quantum wells in the quantum spin Hall regime. *Nature Mater.* **12,** 787–791 (2013).
11. Rugar, D., Budakian, R., Mamin, H. J. & Chui, B. W. Single spin detection by magnetic resonance force microscopy. *Nature* **430,** 329–332 (2004).
12. Degen, C., Poggio, M., Mamin, H., Rettner, C. & Rugar, D. Nanoscale magnetic resonance imaging. *Proc. Natl Acad. Sci. USA* **106,** 1313–1317 (2009).
13. Childress, L. *et al.* Coherent dynamics of coupled electron and nuclear spin qubits in diamond. *Science* **314,** 281–285 (2006).
14. Bar-Gill, N. *et al.* Suppression of spin-bath dynamics for improved coherence of multi-spin-qubit systems. *Nature Commun.* **3,** 858 (2012).
15. Belthangady, C. *et al.* Dressed-state resonant coupling between bright and dark spins in diamond. *Phys. Rev. Lett.* **110,** 157601 (2013).
16. Kolkowitz, S., Unterreithmeier, Q. P., Bennett, S. D. & Lukin, M. D. Sensing distant nuclear spins with a single electron spin. *Phys. Rev. Lett.* **109,** 137601 (2012).
17. Taminiau, T. *et al.* Detection and control of individual nuclear spins using a weakly coupled electron spin. *Phys. Rev. Lett.* **109,** 137602 (2012).
18. Grinolds, M. S. *et al.* Sub-nanometer resolution in three-dimensional magnetic resonance imaging of individual dark spins. *Nature Nanotech.* **9,** 279–284 (2014).
19. Grinolds, M. S. *et al.* Nanoscale magnetic imaging of a single electron spin under ambient conditions. *Nature Phys.* **9,** 215–219 (2013).
20. Loretz, M., Pezzagna, S., Meijer, J. & Degen, C. L. Nanoscale nuclear magnetic resonance with a 1.9-nm-deep nitrogen-vacancy sensor. *Appl. Phys. Lett.* **104,** 033102 (2014).
21. Sushkov, A. O. *et al.* All-optical sensing of a single-molecule electron spin. *Nano Lett.* **14,** 6443–6448 (2014).
22. Le Sage, D. *et al.* Optical magnetic imaging of living cells. *Nature* **496,** 486–489 (2013).
23. Sushkov, A. O. *et al.* Magnetic resonance detection of individual proton spins using quantum reporters. *Phys. Rev. Lett.* **113,** 197601 (2014).
24. Pham, L. M. *et al.* Magnetic field imaging with nitrogen-vacancy ensembles. *New J. Phys.* **13,** 045021 (2011).
25. Gullion, T., Baker, D. B. & Conradi, M. S. New, compensated Carr–Purcell sequences. *J. Magn. Reson.* **89,** 479–484 (1990).
26. de Lange, G., Ristè, D., Dobrovitski, V. V. & Hanson, R. Single-spin magnetometry with multi-pulse dynamical decoupling sequences. *Phys. Rev. Lett.* **106,** 080802 (2011).
27. Naydenov, B. *et al.* Dynamical decoupling of a single-electron spin at room temperature. *Phys. Rev. B* **83,** 081201 (2011).
28. Ryan, C. A., Hodges, J. S. & Cory, D. G. Robust decoupling techniques to extend quantum coherence in diamond. *Phys. Rev. Lett.* **105,** 200402 (2010).
29. Bar-Gill, N., Pham, L. M., Jarmola, A., Budker, D. & Walsworth, R. Solid-state electronic spin coherence time approaching one second. *Nature Commun.* **4,** 1743 (2013).
30. Cywiński, Ł., Lutchyn, R. M., Nave, C. P. & Das Sarma, S. How to enhance dephasing time in superconducting qubits. *Phys. Rev. B* **77,** 174509 (2008).
31. Bylander, J. *et al.* Noise spectroscopy through dynamical decoupling with a superconducting flux qubit. *Nature Phys.* **7,** 565–570 (2011).
32. Hall, L. T., Cole, J. H., Hill, C. D. & Hollenberg, L. C. L. Sensing of fluctuating nanoscale magnetic fields using nitrogen-vacancy centers in diamond. *Phys. Rev. Lett.* **103,** 220802 (2009).
33. Fuller, G. H. *Nuclear Spins and Moments* (American Chemical Society, 1976).
34. Mamin, H. *et al.* Isotope-selective detection and imaging of organic nanolayers. *Nano Lett.* **9,** 3020–3024 (2009).

35. Xue, F., Weber, D. P., Peddibhotla, P. & Poggio, M. Measurement of statistical nuclear spin polarization in a nanoscale GaAs sample. *Phys. Rev. B* **84,** 205328 (2011).
36. Arai, K. *et al.* Fourier magnetic imaging with nanoscale resolution and compressed sensing speed-up using electronic spins in diamond. Preprint at http://arxiv.org/abs/1409.2749 (2014).
37. Kessler, E. M., Lovchinsky, I., Sushkov, A. O. & Lukin, M. D. Quantum error correction for metrology. *Phys. Rev. Lett.* **112,** 150802 (2014).

Acknowledgements

This work was supported by the National Science Foundation and the Defense Advanced Research Projects Agency QuASAR programme. F.C. acknowledges support from the Swiss National Science Foundation. I.L. acknowledges support from a National Defense Science and Engineering Graduate fellowship.

Author contributions

S.J.D.V. and L.M.P. contributed equally to this work. R.L.W., S.J.D., L.M.P. and N.B-G. conceived the idea of the study. S.J.D., L.M.P., I.L., A.O.S. and M.C. performed the measurements and analysed the data. F.C. and S.J.D. developed the model for describing the signal. H.Z. and C.B. created the SiO_2 masks. M.D.L., H.P., R.L.W. and A.Y. conceived the NV-diamond wide-field magnetic imager and its applications. R.L.W. supervised the project. All authors discussed the results and participated in writing the manuscript.

Additional information

Supplementary information is available in the online version of the paper. Reprints and permissions information is available online at www.nature.com/reprints. Correspondence and requests for materials should be addressed to R.L.W.

Competing financial interests

The authors declare no competing financial interests.

ERRATUM

Nanoscale NMR spectroscopy and imaging of multiple nuclear species

Stephen J. DeVience, Linh M. Pham, Igor Lovchinsky, Alexander O. Sushkov, Nir Bar-Gill, Chinmay Belthangady, Francesco Casola, Madeleine Corbett, Huiliang Zhang, Mikhail Lukin, Hongkun Park, Amir Yacoby and Ronald L. Walsworth

Nature Nanotechnology http://dx.doi.org/10.1038/nnano.2014.313 (2015); published online 5 January 2015; corrected online 16 January 2015.

In the version of this Letter originally published online, in Fig. 4f, there was a superfluous blue curve. This error has now been corrected in all versions of the Letter.